Tunable genetic devices through simultaneous control of transcription and translation

Vittorio Bartoli[1,2], Mario di Bernardo[1,2,3] and Thomas E. Gorochowski[1,4,*]

[1] BrisSynBio, University of Bristol, Life Sciences Building, Tyndall Avenue, Bristol, UK

[2] Department of Engineering Mathematics, University of Bristol, Woodland Road, Bristol, UK

[3] Department of Electrical Engineering and Information Technology, University of Naples Federico II, Via Claudio 21, Napoli, Italy

[4] School of Biological Sciences, University of Bristol, Bristol, Tyndall Avenue, UK

* Correspondence should be addressed to T.E.G. (thomas.gorochowski@bristol.ac.uk)

Keywords: gene regulation; genetic circuits; transcription; translation; toehold switch; synthetic biology; systems biology.

Abstract

Synthetic genetic circuits allow us to modify the behavior of living cells. However, changes in environmental conditions and unforeseen interactions between a circuit and the host cell can cause deviations from a desired function, resulting in the need for time-consuming physical re-assembly to fix these issues. Here, we use a regulatory motif controlling transcription and translation to create genetic devices whose response functions can be dynamically tuned. This approach allows us, after assembly, to shift the on and off states of a sensor by 4.5- and 28-fold, respectively, and modify a genetic NOT gate to allow its transition from an on to off state to be varied over a 7-fold range. In both cases, “tuning” leads to trade-offs in the fold-change and separation between the distributions of cells in on and off states. By using mathematical modelling, we derive design principles that are used to further optimize these devices. This work lays the foundation for adaptive genetic circuits that can be tuned after their physical assembly to maintain functionality across diverse environments and design contexts.

Introduction

Gene regulatory networks, or genetic circuits as they are often known, govern when and where genes are expressed in cells and control core biochemical processes like transcription and translation [1,2]. The ability to synthesize DNA encoding engineered genetic circuits offers a means to expand the capabilities of a cell and reprogram its behavior [1,3]. Synthetic genetic circuits have been built to implement computational operations [4–12], dynamic behaviors like oscillations [13–15], and even coordinate multicellular actions across a population [16–20].

The ability to reprogram living cells is simplified by using genetically encoded devices that use common input and output signals [1,2,7,9]. This allows the output of one device to be directly connected to the input of another to create circuits implementing more complex functionalities. Signals can take many forms, but one of the most commonly used is RNA polymerase (RNAP) flux with promoters are used to guide this signal to specific points in a circuit's DNA [7,21]. Based on such input and output signals, the response function of a genetic device captures how inputs map to outputs at steady state [1,7,21]. By ensuring the response functions of two devices are compatible, i.e. they are "matched" such that the range of the output of the first device spans the necessary range of inputs for the second device, larger circuits can be constructed [22]. Matching of components is vital in circuits where devices exhibit switching behaviors (e.g. for Boolean logic) to ensure input signals are sufficiently separated to accurately trigger required transitions between on and off states as signals propagate through the circuit.

Although the use of characterized genetic devices has enabled the automated design of large genetic circuits [7,23], the response functions of these devices are often sensitive to many factors. For example, differences in host physiology due to culturing conditions [24–26] and interactions between genetic parts and the host cell [27–32], can all affect the response function of a device and subsequently its compatibility within a circuit. This makes the creation of reliable and robust genetic circuits a challenge. Even when considering carefully controlled conditions, like those in the lab, a genetic circuit often needs to be reassembled from scratch multiple times using alternative parts until a working combination is found. This is both time consuming and expensive, and often has to be repeated if the circuit is to be deployed in slightly different conditions or host strain.

In this work, we tackle this problem by developing genetic devices whose response functions can be dynamically tuned after physical assembly to correct for unwanted changes in their behavior. The ability to tune/modify the steady state input-output relationship is made possible by employing a simple regulatory motif. We show how this motif can be connected to small molecule sensors to characterize its function and then illustrate how it can be integrated into a genetic NOT gate [33] to allow for the tuning of the transition point between an on and off

state. These capabilities make these devices more broadly compatible with other components [1,7,22], but come at a cost; trade-offs in their performance, i.e. the dynamic range and the ability to differentiate on and off states due to variability in gene expression across a population. We use mathematical modelling to better understand these limitations and derive design principles that are then used to further optimize their design. This work is a step towards genetic circuitry whose individual components can functionally adapt, ensuring robust system-level behaviors are maintained no matter the genetic, cellular or environmental context.

Results

Controlling transcription and translation using a tunable expression system

To allow for the response of a genetic device to be modulated, we developed a tunable expression system (TES) based on a simple regulatory motif where two separate promoters control the transcription and translation rates of a gene of interest (**Figure 1A**). By using promoters as inputs, it is possible to easily connect a TES to existing genetic components/circuitry or even endogenous transcriptional signals within a cell. The TES consists of a toehold switch (THS) that enables the translation initiation rate of the gene of interest to be varied by the relative concentration of a "tuner" small RNA (sRNA) [6,34]. The main component of the THS is a 92 bp DNA sequence that encodes a structural region and a ribosome binding site (RBS) used to drive translation of a downstream protein coding region. This is expressed from a promoter that acts as the main input to the TES (**Figure 1A**). When transcribed, the structural region of the THS mRNA folds to form a hairpin loop secondary structure that makes the RBS less accessible to ribosomes and thus reduces its translation initiation rate. This structure is disrupted by a second component, a 65 nt tuner sRNA that is complementary to the first 30 nt of the THS [34]. The tuner sRNA is expressed from a second promoter, which acts as a tuner input to the device (**Figure 1A**). Complementarity between the tuner sRNA and a short unstructured region of the toehold switch enables initial binding, which then makes it thermodynamically favorable for the sRNA to unfold the secondary structure of the THS through a branch migration process. This increases the accessibility of the RBS and increases the translation initiation rate. Relative concentrations of the THS mRNA and tuner sRNA (controlled by the input and tuner promoters) enables the rate of translation initiation to be potentially varied over a 100-fold range for the toehold switch design we selected for our own [34] (**Materials and Methods**). However, THS designs exist which allow for up to a 400-fold change in translation initiation rates [6,34].

We selected as main and tuner inputs for the TES the output promoters of two sensors, P_{tet} and P_{tac}, that respond to anhydrotetracycline (aTc) and isopropyl β-D-1-thiogalactopyranoside (IPTG), respectively (**Figure 1B**). This allows us to dynamically tune

transcription and translation rates of a gene to modify the overall rate of protein production. Each sensor consists of a transcription factor (TetR and LacI sensitive to aTc and IPTG, respectively) that represses its cognate promoter until an associated small molecule is present (**Figure 1B**). These bind to the transcription factor, altering its conformation and limiting its ability to repress the promoter, thereby turning on transcription of the downstream gene. Yellow fluorescent protein (YFP) was used as the output from the TES (**Figure 1B**) to allow us to measure the rate of protein production in single cells using flow cytometry.

Characterization of the device was performed in *Escherichia coli* cells grown in different concentrations of aTc (input) and IPTG (tuner). Steady state fluorescence measurements of single cells in exponential growth phase were taken using flow cytometry and promoter activities of both the main and tuner input were measured in relative promoter units (RPUs) to allow for direct comparisons (**Materials and Methods**; **Supplementary Figure S1**). For a fixed tuner promoter activity, we observed a sigmoidal increase in output YFP fluorescence as the input promoter activity increased from 0.002 to 6.6 RPU (**Figure 1C**). As the activity of the tuner promoter increased from 0.002 to 2.6 RPU, the entire response function was shifted upwards to higher output YFP fluorescence levels. Notably, this shift was not uniform, with larger relative increases seen for lower input promoter activities; 28-fold versus 4.5-fold for inputs of 0.002 and 6.6 RPU, respectively (**Figure 1C**). Closer analysis of the flow cytometry data (**Figure 1D**), showed that these changes arose from the distributions of output YFP fluorescence for low and high inputs shifting uniformly together as the tuner promoter activity was increased. Therefore, even though a similar relative difference between outputs for low and high inputs (also referred to as the dynamic range) was observed for all tuner inputs, when the tuner input is low, the distributions are virtually identical to the autofluorescence of the cells (**Figure 1D**). This leads to even small absolute differences in the median values between low and high input states resulting in high fold-changes.

To better understand this effect, we derived a deterministic ordinary differential equation (ODE) model of the system (**Supplementary Text S1**). Simulations of this model for biologically realistic parameters (**Supplementary Table S1**) showed similar qualitative behavior to the experiments; increasing turner promoter activity shifted the response curve to higher output protein production rates (**Figure 1E**). However, unlike the experiments, increases in the tuner promoter activity resulted in similar relative increases for low and high inputs (i.e. a similar fold-change). One possible mechanism that could account for the non-linear response observed in the experiments is the limiting effect that the tuner sRNA can have. Because the tuner sRNA concentration is fixed for each response function, its level could be such that it is higher than the concentration of THS transcripts when the main input is low, while being much lower when the main input is high. This would cause the rate of

protein production to be limited by the THS transcript concentration at low inputs, and by the tuner sRNA concentration at high inputs.

Flow cytometry data also showed a significant overlap in the output YFP fluorescence distributions for low and high input promoter activities (**Figure 1D**). Many applications require that "on" and "off" states in a system are well separated so that each can be accurately distinguished (e.g. for Boolean logic). To assess this separation in the TES, we calculated the fractional overlap between the output YFP fluorescence distributions for low and high input promoter activities (**Materials and Methods**). We found a constant intersection of ~70% across all tuner promoter activity levels (**Figure 1F**), which resulted from the near uniform relative shifts we see in output across all input promoter activities.

Design and assembly of a tunable genetic NOT gate

Some genetic devices rely on the expression of proteins such as transcription factors to implement basic logic functions that can be composed to carry out more complex decision-making tasks [4,7,8]. One such commonly used device is a NOT gate, which has a single input and output [33]. The function of this gate is to "invert" the input such that the output is high if the input is low and vice versa. Such a behavior can be implemented by using promoters as the input and output, with the input promoter driving expression of a repressor protein that binds to the DNA of the constitutive output promoter. When the input promoter is inactive, the repressor is not synthesized and so the constitutive output promoter is active. However, once the input promoter is activated, the repressor is expressed which binds the output promoter and represses its activity.

Because the activity range of promoters varies, the transition point whereby sufficient concentrations of repressor are present to cause strong repression of the output promoter may make it impossible to connect other devices and ensure a signal is correctly propagated. For example, the output promoter of a weak sensor system acting as input to a NOT gate with a high transition point might lead to insufficient production of the repressor causing the output promoter to be continually active. These incompatibilities can sometimes be corrected for by modifying other regulatory elements in the design. In the case of a repressor-based NOT gate, while the promoters cannot be easily changed, in bacteria the translation initiation rate can be varied by altering the ribosome binding site (RBS) for the repressor gene. Increasing the RBS strength causes more repressor protein to be produced for the same input promoter activity, shifting the transition point to a lower value [7,33]. While such modifications can fix issues with device compatibility, they require reassembly of the entire genetic device.

Given that the TES allows for the rates of both transcription and translation to be dynamically controlled, we attempted to create a proof-of-concept "tunable" NOT gate that integrated the TES to allow its response function, and crucially the transition point, to be

altered after physical assembly. We chose an existing NOT gate design [33] that uses the PhlF repressor to control the activity of the output P_{phlF} promoter (**Figure 2A**). Expression of PhlF was controlled by the TES (replacing the YFP reporter protein in the original TES design; **Figure 1A**). Unlike the TES, the tunable NOT gate uses promoters for both inputs and outputs allowing it to be easily connected to other devices that use RNAP flux as an input/output signal (**Figure 2A**).

To enable characterization of the tunable NOT gate, the output promoter P_{phlF} was used to drive expression of YFP. Measurements were taken using flow cytometry for cells harboring the device in varying concentrations of aTc and IPTG, and steady state response functions generated (**Figures 2B** and **2C**). As expected, these displayed a negative sigmoidal shape with transition points (*K* values from the Hill function fits to the experimental data) that varied over a 7-fold range (**Figure 2B**). We also found that increases in the tuner promoter activity lead to transitions at lower activity levels for the input promoter. The range of transition points achieved by our device also covered a high proportion (35%) of the largest collection of repressor-based NOT gates built to date (total of 20 variants; **Figure 2D**) [7].

These results demonstrate the ability of the proposed TES component to dynamically alter a key characteristic of a NOT gate's response function (specifically the transition point) to improve its compatibility with other genetic devices. However, it came at a cost; tuning resulted in a drop in the fold-change between low and high outputs (**Figure 2E**) and an increase in the overlap of the output YFP fluorescence distributions, which made high and low states difficult to distinguish (**Figure 2F**).

Boosting sRNA levels improves the performance of the tunable genetic devices

For the THS to function correctly, it is essential that the sRNA reaches a sufficiently high concentration relative to the THS transcript to ensure the associated RBS is in a predominantly unfolded state [34]. In our design, the tuner input promoter P_{tac} has less than half the maximum strength of the main input promoter P_{tet} (**Supplementary Figure S1**). Furthermore, although the tuner sRNA contains a hairpin to improve its stability, sRNAs are generally more quickly turned over than normal transcripts [35,36], yielding much lower steady state concentrations compared to the THS transcript.

To better understand the role that the THS transcript to tuner sRNA ratio had on the performance of the TES, we used our mathematical model of the system (**Supplementary Text S1**) to explore how various key parameters (e.g. transcription rates and binding affinities) altered the response function of the device. Using biologically realistic ranges of parameters (**Supplementary Table S1**), we found that for lower sRNA transcription rates the output response function could be shifted maintaining a similar fold-change between low and high output states (**Figure 3A**). At these low THS/sRNA ratios the translation rate from the THS

transcript is limited by the sRNA concentration. However, as the sRNA transcription rate increased a transition point was seen (i.e. between green and blue shared curves in **Figure 3A**) whereby for low THS transcription rates the sRNAs are in excess making the output protein production rate limited by the THS transcript concentration (**Figure 3A**). In contrast, at high THS transcription rates the sRNAs become limiting again but allow for relatively much higher output protein production rates that enable a larger fold-change in the response function of the TES (**Figure 3A**). Further stochastic modelling of the system showed that increased sRNA transcription rates also reduced variability in the distribution of protein production rates across a population and lowered the fractional intersection between low and high output states (**Figure 3B**).

To experimentally verify the benefit of increasing the sRNA transcription rate, we built a complementary sRNA booster plasmid that contained a high-copy pColE1 origin of replication (50–70 copies per cell) [37] and expressed the tuner sRNA from a strong viral P_{T7} promoter (**Figure 3C**) [38]. Transcription from P_{T7} requires T7 RNA polymerase (T7RNAP). This is provided by our host strain *E. coli* BL21 Star (DE3), which has the *T7RNAP* gene under the control of an IPTG inducible P_{lacUV5} promoter within its genome (**Figure 3C**) [39]. Induction of the tuner P_{tac} promoter in our devices using IPTG leads to simultaneous expression of T7 RNAP from the host genome and transcription of additional tuner sRNA from the booster plasmid (**Figure 3C**). As the tunable devices are encoded on a plasmid with a p15A origin of replication (~15 copies per cell; **Supplementary Figure S2**) [40], we would expect at least five times higher tuner sRNA concentrations are reached when the sRNA booster is present.

Cells were co-transformed with each tunable genetic device and sRNA booster plasmid, and their response functions were measured (**Figures 3D** and **3E**). As predicted by the modelling, the TES displayed improved performance with a more than doubling in the fold-change across all tuner promoter activities and >40% drop in the intersection between low and high output YFP fluorescence distributions (**Table 1**). For the tunable NOT gate only minor differences in performance were seen with mostly decreases for high tuner promoter activities.

Self-cleaving ribozyme insulators impact toehold switch function

In our initial designs, a RiboJ self-cleaving ribozyme was included in the TES and NOT gate to insulate the translation of the *yfp* or *phlF* genes, respectively, from different 5' untranslated region (UTR) sequences that might be generated when using different promoters as an input (**Figures 1A, 2A**) [41]. Any variable UTR sequences would be cleaved at the RiboJ site to produce a standardized mRNA with more consistent rates of mRNA degradation and translation. Unfortunately, because RiboJ contains a number of strong secondary RNA structures [41,42], it is possible that the 23 nt hairpin at the 3'-end impacts the ability for the sRNA to interact with the THS, reducing the hybridization rate (**Figure 4A**).

To assess whether the RiboJ insulator might affect the stability of secondary structures that are crucial to the TES's function, we performed thermodynamic modelling of the binding between the toehold switch region of the mRNA and the tuner sRNA for variants of the TES design with and without RiboJ present (**Materials and Methods**). Simulations showed a 40% drop in the predicted Gibbs free energy of the reactants when RiboJ was removed (−40.5 kcal/mol with versus −65 kcal/mol without RiboJ; **Figure 4B**). This suggests that binding of the sRNA may be hampered by interactions with the RiboJ insulator, lowering the effective translation initiation rate of the RBS controlled by the toehold switch and subsequently the overall performance of the devices.

To experimentally test these predictions, non-insulated variants of the TES and tunable NOT gate were constructed in which RiboJ was removed. Characterization of these devices showed major improvements in overall performance (**Figures 4C** and **4D**). The TES saw more than a doubling in the dynamic range and 10-fold increase in the fold-change between on and off states across low and high tuner activity levels compared to the original design and a >50% drop in the fraction of intersection of the output YFP fluorescence distributions (**Table 1**). The tunable NOT gate saw more modest improvements with a 73% increase in the fold-change at high tuner activity levels, but an overall drop of 66% in the range of transition points (K values) that could be achieved (**Table 1**). These results highlight an important consideration often ignored. When using RNA-based devices that require proper formation of secondary structures, care must be taken in looking at how multiple devices relying on mRNA folding to function could interfere with each other, leading to cryptic failure modes.

Another counterintuitive change in the TES's response function after RiboJ removal was the large drop in output YFP fluorescence from 26 to 3 arbitrary units (a.u.) when no input or tuner was present (**Figure 4C**). Similar drops were also seen of between 4- and 11-fold for higher tuner promoter activities. Given that binding of a tuner sRNA to the THS mRNA should be less hampered without RiboJ present, an increase not decrease in output protein production would be expected. A possible explanation is that the stability of the THS mRNA decreases after the removal of RiboJ. This is supported by recent results that have shown the RiboJ insulator both stabilizes its mRNA and also boost the translation initiation rate of a nearby downstream RBS [43]. The precise mechanisms for this are not well understood, but the structural aspect of the RiboJ element at the 5'-end of an mRNA likely inhibits degradation by exonucleases and the hairpin at the 3'-end of RiboJ is thought to help expose the nearby RBS by reducing the chance of secondary structure formation [41,42].

Finally, we combined the non-insulated designs with the sRNA booster plasmid to see whether further improvements could be made (**Table 1**). For the TES, we found that the dynamic range had plateaued, with only moderate increases that were mostly at low tuner promoter activities. In contrast, the fold-change between low and high outputs more than

doubled across tuner promoter activities when compared to the non-insulated design, and a further drop of >18% was seen in the fractional intersection between the YFP fluorescence distributions for these output states. The tunable NOT gate showed minor decreases in performance for many of the measures (**Table 1**). However, the inclusion of the sRNA booster likely increased overall PhlF concentrations as the transition points from an on to off state (*K* value range) shifted to far below what had been seen for all other designs. This would make this specific design of value for uses where a weak input signal needs to be inverted and amplified simultaneously.

Discussion

In this work, we have developed a new class of genetic device where an additional tuner input is able to dynamically change key features of the device's response function. This was achieved by employing a regulatory motif that allows for the transcription and translation rate of a gene to be controlled by the activity of multiple input promoters. Connecting this TES to a number of small molecule sensors, we were able to demonstrate its ability to shift the on and off output states by 4.5- and 28-fold, respectively (**Figure 1**). Furthermore, we showed how the TES could be incorporated into a genetic NOT gate to enable tuning of the crucial transition point between an on and off state over a 7-fold range (**Figure 2**). This made the gate more broadly compatible with other components where matching of transition points to high and low output levels is essential for effective propagation of biological computations [7,22]. Unfortunately, the performance of the tunable sensor and NOT gate varied for differing tuner inputs, leading to a trade-off between performance and the level of tuning required. Mathematical and biophysical modelling of the TES helped to uncover: 1. the importance of ensuring sufficient tuner sRNA is present to fully activate the THS (**Figure 3**), and 2. the presence of possible detrimental interactions between a self-cleaving ribosome used to insulate protein expression from genetic contextual and the THS that relies on the correct folding of an RNA secondary structure to function properly (**Figure 4**). Modified designs that addressed these concerns demonstrated improved performance for the TES in both cases, but only minor improvements in the fold-change of the tunable NOT gate when the self-cleaving ribosome was removed (**Table 1**). By combining these two modifications into a single system, further improvements were also observed for the TES, but not the tunable NOT gate when compared to the original designs (**Table 1**). To our knowledge the simultaneous control of transcription and translation to tune the response function of a genetic device has not been shown before, making this work a valuable resource for others to build on. Furthermore, unlike other attempts at tuning the response of devices through mutation of protein components to

alter catalytic rates [44], our method allows for dynamic changes to a response function using simple to control transcriptional signals (i.e. by the use of appropriate promoters).

An interesting future direction opened up by the adaptive nature of our devices is the ability to incorporate many of them into larger circuits. This would allow many parts of a circuit to be tuned simultaneously to maximize the compatibility between components and optimize the behavior of the overall system. Unlike a typical design-build-test cycle that requires the reassembly of a genetic circuit with a new combination of parts if malfunctions are detected, this work supports a design-build-test-*tune* cycle where time consuming and costly reassembly can be avoided. Rather than reassembling a circuit after each cycle, parts can instead be dynamically tuned until they work correctly in unison. In this context, the use of sensitivity analysis [45], during circuit design would offer valuable insight into specific components where even small deviations in behavior would adversely impact overall circuit function. These would be ideal candidates to be encoded using tunable devices to allow for tweaking at these critical points. Furthermore, the use of new microfluidic culturing systems and online machine learning algorithms offers a way to rapidly discover the precise tuner inputs needed to achieve specific circuit functions under fluctuating environmental conditions [46–49].

Some practical challenges are raised by the additional tuner input in our devices. Systems composed of numerous tunable devices will require a large number of tuner inputs to be controlled simultaneously. If external signals are to be used, then a unique sensor is required for each tuner input as well as the capability to be able to control the environment to provide the correct set of input signals over time. Although the range of small molecule [50] and light based [44,51] sensing systems available to bioengineers in *E. coli* has grown over recent years, the ability to control many environmental factors (e.g. small molecule concentrations and light intensities) simultaneously remains difficult. However, external control is not the only way to tune the behavior of these devices. The use of promoters as inputs and outputs allows them to be controlled by connecting them directly to the many transcriptional signals used natively in a cell. This offers the advantage of tapping into the cells innate capacity to sense and respond to its environment and internal protein synthesis demands.

For synthetic biology to have a broad and lasting impact outside of the carefully controlled conditions of a lab, it is vital that means are developed to construct adaptive genetic circuits able to maintain their functionality when exposed to unexpected environmental changes or shifts in host cell physiology [52]. By combining advances in biological control engineering [52–57] with the tunable genetic devices developed in this work, bioengineers have a complementary set of tools capable of taking steps towards this goal.

Materials and Methods

Strains and media

Cloning was performed using *Escherichia coli* strain DH5-α (F^- *endA*1 *glnV*44 thi-1 *recA*1 *relA*1 *gyrA*96 *deoR nupG purB*20 φ80d*lacZ*ΔM15 Δ(*lacZYA–argF*)U169, *hsdR*17($r_K^-m_K^+$), λ^-) (New England Biolabs, C2987I). Device characterization was performed using BL21 Star (DE3) (F^- *ompT hsdS*$_B$ (r_B^-, m_B^-) *gal dcm rne*-131 [DE3]) (Thermo Fisher Scientific, C601003). For cloning, cells were grown in LB Miller broth (Sigma-Aldrich, L3522). For device characterization, cells were grown in M9 minimal media supplemented with glucose containing M9 salts (6.78 g/L Na_2HPO_4, 3 g/L KH_2PO_4, 1 g/L NH_4Cl, 0.5 g/L NaCl) (Sigma-Aldrich, M6030), 0.34 g/L thiamine hydrochloride (Sigma T4625), 0.4% D-glucose (Sigma-Aldrich, G7528), 0.2% casamino acids (Acros, AC61204-5000), 2 mM $MgSO_4$ (Acros, 213115000), and 0.1 mM $CaCl_2$ (Sigma-Aldrich, C8106). Antibiotic selection was performed using 50 μg/mL kanamycin (Sigma-Aldrich, K1637) or 50 mg/mL spectinomycin (Santa Cruz Biotechnology, sc-203279). Induction of sensor systems was performed using anhydrotetracycline (aTc) (Sigma-Alrdich, 37919) and isopropyl β-D-1-thiogalactopyranoside (IPTG) (Sigma-Aldrich, I6758).

Genetic device synthesis and assembly

Plasmids containing the TES and tunable NOT gate devices were constructed by gene synthesis of the individual transcriptional units (e.g. tuner sRNA, THS-*yfp*, THS-*phlF* and *yfp*), (GeneArt, Thermo Fisher Scientific) and insertion of these elements into a pAN1201 plasmid backbone. pAN1201 provides all the sensor systems used for induction of the input promoters. Assembly was performed by first PCR of the synthesized transcriptional units and the pAN1201 plasmid (without the *lacZα* region normally used for blue/white screening) with all primers containing a 20 bp tail homologous sequence to the previous or subsequent region in the desired assembly. Gibson assembly (New England Biolabs, E2611S) was then used to scarlessly assemble these fragments into a complete plasmid. The plasmid used to boost tuner sRNA levels (pVB005) was fully synthesized (GeneArt, Thermo Fisher Scientific). Annotated plasmid maps of all devices are provided in **Supplementary Figure S2** and **Supplementary File S2**. All plasmids were sequence verified by Sanger sequencing (Eurofins Genomics).

Genetic device characterization

Single colonies of cells transformed with the appropriate genetic constructs were inoculated in 200 μL M9 media supplemented with glucose and necessary antibiotics for selection in a 96-well microtiter plate (Thermo Fisher Scientific, 249952) and grown for 16 hours in a shaking incubator (Stuart, S1505) at 37 °C and 1250 rpm. Following this, cultures were diluted 9:1600 (15 μL into 185 μL, with 15 μL of this dilution loaded into 185 μL) in glucose supplemented M9

media with necessary antibiotics for selection and grown for 3 hours at the same conditions. Next, the cultures were diluted 1:45 (10 µL into 140 µL) into supplemented M9 media with necessary antibiotics for selection and any required inducers in a new 96-well microtiter plate (Thermo Fisher Scientific, 249952) and grown at 37 °C and 1250 rpm for 5 hours. Finally, the cells were diluted 1:10 (10 µL into 90 µL) in phosphate-buffered saline (PBS) (Gibco,18912-014) containing 2 mg/mL kanamycin to halt translation and incubated at room temperature for 1 hour to allow for maturation of the YFP before performing flow cytometry.

Flow cytometry

YFP fluorescence of individual cells was measured using an Acea Biosciences NovoCyte 3000 flow cytometer equipped with a NovoSampler to allow for automated collection from 96-well microtiter plates. Cells were excited using a 488 nm laser and measurements taken using a 530 nm detector. A flow rate of 40 µL/min was used to collect at least 10^5 cells for all measured conditions. Automated gating of events using the forward (FSC-A) and side scatter (SSC-A) channels was performed for all data using the FlowCal Python package version 1.2 [58] and the density2d function with parameters: channels = ['FSC-A', 'SSC-A'], bins = 1024, gate_fraction = 0.5, xscale = 'logicle', yscale = 'logicle', and sigma = 10.0.

Autofluorescence correction

To measure YFP fluorescence from our constructs it was necessary to correct for the autofluorescence of cells. An autofluorescence control strain containing the pAN1201 plasmid [7], which does not express YFP but contains the same backbone as our genetic devices, was measured using flow cytometry under the same culturing conditions as for characterization. Measurements were taken from three biological replicates and an average of the medians of the gated distributions was subtracted from the gated YFP fluorescence flow cytometry data of the characterized devices, as in previous work [7].

Characterization of sensor systems in relative promoter units (RPU)

To allow for inputs to our devices to be controlled in standardized relative promoter units (RPUs) [7,59], calibration curves for the two sensor systems were generated to enable a conversion between a chemical inducer concentration and the relative promoter activity of each sensors' output promoter (P_{tac} and P_{tet}). Cells transformed with plasmids pAN1718 and pAN1719 for P_{tac} and P_{tet}, respectively, and the pAN1717 RPU standard [7], were cultured in the same way as the characterization experiments. Flow cytometry was used to measure YFP fluorescence which was further corrected for cell autofluorescence. RPU values were then calculated by dividing the YFP output from the sensor by the YFP output from the RPU standard and a Hill function fitted to the resultant data (**Supplementary Figure S1**).

417

418 ***Quantifying histogram intersections***

419 The fraction of intersection *H* between two histograms (e.g. flow cytometry fluorescence
420 distributions), *x* and *y*, was calculated using,

421 $$H(x,y) = \sum_{i=1}^{n} \frac{\min(x_i, y_i)}{x_i}. \quad (1)$$

422 Here, histograms *x* and *y* are divided into *n* bins that correspond to identical ranges of values
423 for each, with x_i and y_i denoting the value of bin *i* for histogram *x* or *y*, respectively.

424

425 ***Predicting RNA binding and secondary structure***

426 To predict the binding and secondary structure of the toehold switch and tuner sRNA (**Figure**
427 **3**), thermodynamic modelling was performed using the NUPACK web application [60]. All
428 simulations were run using the parameters: nucleic acid = RNA, temperature = 37 °C and the
429 concentration of toehold switch mRNA was set to 5×10^{-4} μM. The switch sequence mRNA
430 and the switch sequence mRNA with an upstream cleaved RiboJ were simulated
431 independently with additional parameters strand species = 1 and a maximum complex size =
432 1. The toehold switch mRNA with and without an upstream RiboJ sequence where also
433 simulated in the presence of trigger sRNA set to a concentration of 7×10^{-5} μM with additional
434 parameters: strand species = 1 and a maximum complex size = 1. Full sequences are given
435 in **Supplementary Table S2**.

436

437 ***Computational analyses and data fitting***

438 All computational analyses were performed using Python version 3.6.6. Response functions
439 for the TES designs were generated by fitting median values of YFP fluorescence from flow
440 cytometry data to a Hill function of the form

441 $$y = y_{\min} + (y_{\max} - y_{\min}) \frac{x^n}{K^n + x^n}, \quad (2)$$

442 where *y* is the output YFP fluorescence (in arbitrary units), y_{min} and y_{max} are the minimum and
443 maximum output YFP fluorescence (in arbitrary units), respectively, *K* is the input promoter
444 activity (in RPU units) at which the output is halfway between its minimum and maximum, *n* is
445 the Hill coefficient, and *x* is the input promoter activity (in RPU units). Response functions for
446 the tunable NOT gates were generated in a similar way using a Hill function of the form

447 $$y = y_{\min} + (y_{\max} - y_{\min}) \frac{K^n}{K^n + x^n}. \quad (3)$$

448 Fitting of data was performed using non-linear least squares and the curve_fit function from
449 the SciPy.integrate Python package version 1.1.

450

451 ***Numerical simulation***

The deterministic ODE model (**Supplementary Text S1**) was simulated using the odeint function of the SciPy.integrate Python package version 1.1 with default parameters. Stochastic simulations of biochemical model (**Supplementary Text S1**) were performed using the tau-leap method in COPASI [61] version 4.24 with the settings: duration = 100 min, interval size = 1 min, number of intervals = 100 and starting in steady state.

Visualization of genetic designs

All genetic diagrams are shown using Synthetic Biology Open Language Visual (SBOL Visual) notation [62]. SBOL Visual diagrams were generated using the DNAplotlib Python package [63,64] version 1.0 which were then annotated and composed with OmniGraffle version 7.9.2.

Data availability

Systems Biology Markup Language (SBML) files implementing models of the TES and tunable NOT gate can be found in **Supplementary File S1**. Annotated sequence files in GenBank format for all plasmids are available in **Supplementary File S2**. All plasmids are available from Addgene (#127185–127189).

Acknowledgements

This work was supported by BrisSynBio, a BBSRC/EPSRC Synthetic Biology Research Centre grant BB/L01386X/1 (M.d.B., T.E.G.), EPSRC/BBSRC Centre for Doctoral Training in Synthetic Biology grant EP/L016494/1 (V.B.), the EU Horizon 2020 research project COSY-BIO grant 766840 (M.d.B), and a Royal Society University Research Fellowship grant UF160357 (T.E.G.)

Author Contributions

T.E.G. conceived of the study. V.B. and T.E.G. performed the experiments. V.B. and M.d.B. developed the mathematical models. V.B. analyzed the data. All authors helped write the manuscript.

Conflicts of Interest

The authors declare no competing financial interests.

References

1. Brophy, J. A. N. & Voigt, C. A. Principles of genetic circuit design. *Nat. Methods* **11**, 508 (2014).
2. Greco, F. V., Tarnowski, M. J. & Gorochowski, T. E. Living computers powered by biochemistry. *The Biochemist* **41**, 14–18 (2019).
3. Slomovic, S., Pardee, K. & Collins, J. J. Synthetic biology devices for in vitro and in vivo diagnostics. *Proc. Natl. Acad. Sci.* **112**, 14429 (2015).
4. Andrews, L. B., Nielsen, A. A. K. & Voigt, C. A. Cellular checkpoint control using programmable sequential logic. *Science* **361**, eaap8987 (2018).
5. Bashor, C. J. *et al.* Complex signal processing in synthetic gene circuits using cooperative regulatory assemblies. *Science* **364**, 593 (2019).
6. Green, A. A. *et al.* Complex cellular logic computation using ribocomputing devices. *Nature* **548**, 117 (2017).
7. Nielsen, A. A. K. *et al.* Genetic circuit design automation. *Science* **352**, aac7341 (2016).
8. Moon, T. S., Lou, C., Tamsir, A., Stanton, B. C. & Voigt, C. A. Genetic programs constructed from layered logic gates in single cells. *Nature* **491**, 249 (2012).
9. Gao, X. J., Chong, L. S., Kim, M. S. & Elowitz, M. B. Programmable protein circuits in living cells. *Science* **361**, 1252 (2018).
10. Daniel, R., Rubens, J. R., Sarpeshkar, R. & Lu, T. K. Synthetic analog computation in living cells. *Nature* **497**, 619 (2013).
11. Fernandez-Rodriguez, J., Yang, L., Gorochowski, T. E., Gordon, D. B. & Voigt, C. A. Memory and Combinatorial Logic Based on DNA Inversions: Dynamics and Evolutionary Stability. *ACS Synth. Biol.* **4**, 1361–1372 (2015).
12. Hsiao, V., Hori, Y., Rothemund, P. W. & Murray, R. M. A population-based temporal logic gate for timing and recording chemical events. *Mol. Syst. Biol.* **12**, 869 (2016).
13. Elowitz, M. B. & Leibler, S. A synthetic oscillatory network of transcriptional regulators. *Nature* **403**, 335–338 (2000).
14. Stricker, J. *et al.* A fast, robust and tunable synthetic gene oscillator. *Nature* **456**, 516 (2008).
15. Niederholtmeyer, H. *et al.* Rapid cell-free forward engineering of novel genetic ring oscillators. *eLife* **4**, e09771 (2015).
16. Kong, W., Meldgin, D. R., Collins, J. J. & Lu, T. Designing microbial consortia with defined social interactions. *Nat. Chem. Biol.* **14**, 821–829 (2018).
17. Karig, D. *et al.* Stochastic Turing patterns in a synthetic bacterial population. *Proc. Natl. Acad. Sci.* **115**, 6572–6577 (2018).

18. Cao, Y. *et al.* Programmable assembly of pressure sensors using pattern-forming bacteria. *Nat. Biotechnol.* **35**, 1087–1093 (2017).
19. Danino, T., Mondragón-Palomino, O., Tsimring, L. & Hasty, J. A synchronized quorum of genetic clocks. *Nature* **463**, 326–330 (2010).
20. Din, M. O. *et al.* Synchronized cycles of bacterial lysis for in vivo delivery. *Nature* **536**, 81–85 (2016).
21. Canton, B., Labno, A. & Endy, D. Refinement and standardization of synthetic biological parts and devices. *Nat. Biotechnol.* **26**, 787 (2008).
22. P. Vaidyanathan *et al.* A Framework for Genetic Logic Synthesis. *Proc. IEEE* **103**, 2196–2207 (2015).
23. Weinberg, B. H. *et al.* Large-scale design of robust genetic circuits with multiple inputs and outputs for mammalian cells. *Nat. Biotechnol.* **35**, 453 (2017).
24. Moser, F. *et al.* Genetic Circuit Performance under Conditions Relevant for Industrial Bioreactors. *ACS Synth. Biol.* **1**, 555–564 (2012).
25. Gorochowski, T. E., van den Berg, E., Kerkman, R., Roubos, J. A. & Bovenberg, R. A. L. Using Synthetic Biological Parts and Microbioreactors to Explore the Protein Expression Characteristics of Escherichia coli. *ACS Synth. Biol.* **3**, 129–139 (2014).
26. Cardinale, S. & Arkin, A. P. Contextualizing context for synthetic biology – identifying causes of failure of synthetic biological systems. *Biotechnol. J.* **7**, 856–866 (2012).
27. Gyorgy, A. *et al.* Isocost Lines Describe the Cellular Economy of Genetic Circuits. *Biophys. J.* **109**, 639–646 (2015).
28. Gorochowski, T. E., Avcilar-Kucukgoze, I., Bovenberg, R. A. L., Roubos, J. A. & Ignatova, Z. A Minimal Model of Ribosome Allocation Dynamics Captures Trade-offs in Expression between Endogenous and Synthetic Genes. *ACS Synth. Biol.* **5**, 710–720 (2016).
29. Qian, Y., Huang, H.-H., Jiménez, J. I. & Del Vecchio, D. Resource Competition Shapes the Response of Genetic Circuits. *ACS Synth. Biol.* **6**, 1263–1272 (2017).
30. Yeung, E. *et al.* Biophysical Constraints Arising from Compositional Context in Synthetic Gene Networks. *Cell Syst.* **5**, 11-24.e12 (2017).
31. Gorochowski, T. E. *et al.* Genetic circuit characterization and debugging using RNA-seq. *Mol. Syst. Biol.* **13**, 952 (2017).
32. Gorochowski, T. E. *et al.* Absolute quantification of translational regulation and burden using combined sequencing approaches. *Mol. Syst. Biol.* **15**, e8719 (2019).
33. Stanton, B. C. *et al.* Genomic mining of prokaryotic repressors for orthogonal logic gates. *Nat. Chem. Biol.* **10**, 99–105 (2014).
34. Green, A. A., Silver, P. A., Collins, J. J. & Yin, P. Toehold Switches: De-Novo-Designed Regulators of Gene Expression. *Cell* **159**, 925–939 (2014).

35. Chen, H., Shiroguchi, K., Ge, H. & Xie, X. S. Genome-wide study of mRNA degradation and transcript elongation in Escherichia coli. *Mol. Syst. Biol.* **11**, 781 (2015).
36. Busi, F., Arluison, V. & Régnier, P. Absolute Regulatory Small Noncoding RNA Concentration and Decay Rates Measurements in Escherichia coli. in *Bacterial Regulatory RNA: Methods and Protocols* (eds. Arluison, V. & Valverde, C.) 231–248 (Springer New York, 2018). doi:10.1007/978-1-4939-7634-8_14
37. Lutz, R. & Bujard, H. Independent and Tight Regulation of Transcriptional Units in Escherichia Coli Via the LacR/O, the TetR/O and AraC/I1-I2 Regulatory Elements. *Nucleic Acids Res.* **25**, 1203–1210 (1997).
38. Dunn, J. J., Studier, F. W. & Gottesman, M. Complete nucleotide sequence of bacteriophage T7 DNA and the locations of T7 genetic elements. *J. Mol. Biol.* **166**, 477–535 (1983).
39. Studier, F. W. & Moffatt, B. A. Use of bacteriophage T7 RNA polymerase to direct selective high-level expression of cloned genes. *J. Mol. Biol.* **189**, 113–130 (1986).
40. Hiszczyńska-Sawicka, E. & Kur, J. Effect of Escherichia coli IHF Mutations on Plasmid p15A Copy Number. *Plasmid* **38**, 174–179 (1997).
41. Lou, C., Stanton, B., Chen, Y.-J., Munsky, B. & Voigt, C. A. Ribozyme-based insulator parts buffer synthetic circuits from genetic context. *Nat. Biotechnol.* **30**, 1137 (2012).
42. Carrier, T. A. & Keasling, J. D. Engineering mRNA stability in E. coli by the addition of synthetic hairpins using a 5′ cassette system. *Biotechnol. Bioeng.* **55**, 577–580 (1997).
43. Clifton, K. P. *et al.* The genetic insulator RiboJ increases expression of insulated genes. *J. Biol. Eng.* **12**, 23 (2018).
44. Landry, B. P., Palanki, R., Dyulgyarov, N., Hartsough, L. A. & Tabor, J. J. Phosphatase activity tunes two-component system sensor detection threshold. *Nat. Commun.* **9**, 1433 (2018).
45. Feng, X. *et al.* Optimizing Genetic Circuits by Global Sensitivity Analysis. *Biophys. J.* **87**, 2195–2202 (2004).
46. Postiglione, L. *et al.* Regulation of Gene Expression and Signaling Pathway Activity in Mammalian Cells by Automated Microfluidics Feedback Control. *ACS Synth. Biol.* **7**, 2558–2565 (2018).
47. Menolascina, F. *et al.* In-Vivo Real-Time Control of Protein Expression from Endogenous and Synthetic Gene Networks. *PLOS Comput. Biol.* **10**, e1003625 (2014).
48. Bandiera, L. *et al.* On-Line Optimal Input Design Increases the Efficiency and Accuracy of the Modelling of an Inducible Synthetic Promoter. *Processes* **6**, (2018).
49. Milias-Argeitis, A., Rullan, M., Aoki, S. K., Buchmann, P. & Khammash, M. Automated optogenetic feedback control for precise and robust regulation of gene expression and cell growth. *Nat. Commun.* **7**, 12546 (2016).

50. Meyer, A. J., Segall-Shapiro, T. H., Glassey, E., Zhang, J. & Voigt, C. A. Escherichia coli “Marionette” strains with 12 highly optimized small-molecule sensors. *Nat. Chem. Biol.* **15**, 196–204 (2019).
51. Baumschlager, A., Aoki, S. K. & Khammash, M. Dynamic Blue Light-Inducible T7 RNA Polymerases (Opto-T7RNAPs) for Precise Spatiotemporal Gene Expression Control. *ACS Synth. Biol.* **6**, 2157–2167 (2017).
52. Segall-Shapiro, T. H., Sontag, E. D. & Voigt, C. A. Engineered promoters enable constant gene expression at any copy number in bacteria. *Nat. Biotechnol.* **36**, 352 (2018).
53. Aoki, S. K. *et al.* A universal biomolecular integral feedback controller for robust perfect adaptation. *Nature* **570**, 533–537 (2019).
54. D. Fiore, A. Guarino & M. di Bernardo. Analysis and Control of Genetic Toggle Switches Subject to Periodic Multi-Input Stimulation. *IEEE Control Syst. Lett.* **3**, 278–283 (2019).
55. Mishra, D., Rivera, P. M., Lin, A., Del Vecchio, D. & Weiss, R. A load driver device for engineering modularity in biological networks. *Nat. Biotechnol.* **32**, 1268 (2014).
56. Del Vecchio, D., Abdallah, H., Qian, Y. & Collins, J. J. A Blueprint for a Synthetic Genetic Feedback Controller to Reprogram Cell Fate. *Cell Syst.* **4**, 109-120.e11 (2017).
57. Ceroni, F. *et al.* Burden-driven feedback control of gene expression. *Nat. Methods* **15**, 387–393 (2018).
58. Castillo-Hair, S. M. *et al.* FlowCal: A User-Friendly, Open Source Software Tool for Automatically Converting Flow Cytometry Data from Arbitrary to Calibrated Units. *ACS Synth. Biol.* **5**, 774–780 (2016).
59. Kelly, J. R. *et al.* Measuring the activity of BioBrick promoters using an in vivo reference standard. *J. Biol. Eng.* **3**, 4 (2009).
60. Zadeh, J. N. *et al.* NUPACK: Analysis and design of nucleic acid systems. *J. Comput. Chem.* **32**, 170–173 (2011).
61. Hoops, S. *et al.* COPASI—a COmplex PAthway SImulator. *Bioinformatics* **22**, 3067–3074 (2006).
62. Madsen Curtis *et al.* Synthetic Biology Open Language Visual (SBOL Visual) Version 2.1. *J. Integr. Bioinforma.* (2019). doi:10.1515/jib-2018-0101
63. Der, B. S. *et al.* DNAplotlib: Programmable Visualization of Genetic Designs and Associated Data. *ACS Synth. Biol.* **6**, 1115–1119 (2017).
64. Bartoli, V., Dixon, D. O. R. & Gorochowski, T. E. Automated Visualization of Genetic Designs Using DNAplotlib. in *Synthetic Biology: Methods and Protocols* (ed. Braman, J. C.) 399–409 (Springer New York, 2018). doi:10.1007/978-1-4939-7795-6_22
65. Chen, Y.-J. *et al.* Characterization of 582 natural and synthetic terminators and quantification of their design constraints. *Nat. Methods* **10**, 659 (2013).

Figure and Captions

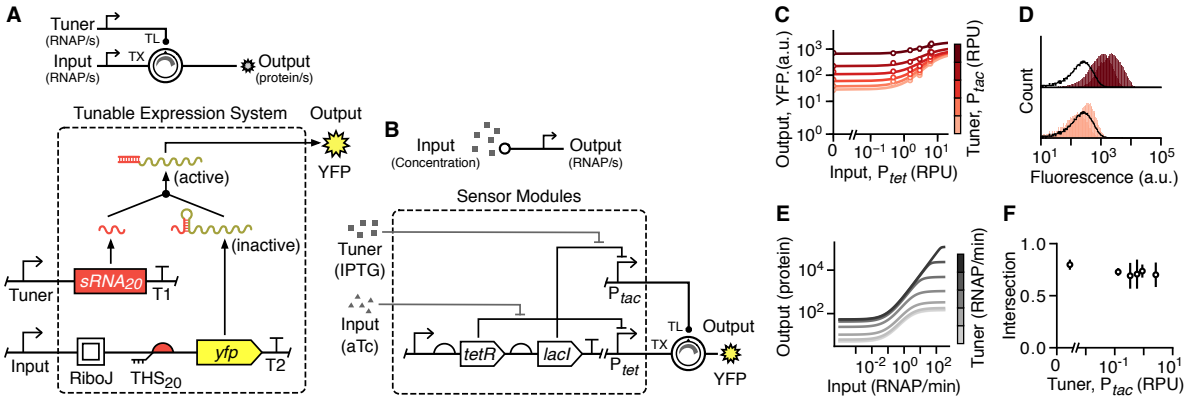

Figure 1: Design and characterization of a tunable expression system (TES). (**A**) Schematic of the TES (top) and genetic implementation using a toehold switch (design 20) [34] to regulate translation initiation rate of an output protein (bottom). Transcriptional (TX) and translational (TL) steps are explicitly shown by arrows within the TES (dashed box). Yellow fluorescent protein (YFP) is used as the output and T1 and T2 correspond to the transcriptional terminators L3S3P11 and L3S2P21, respectively [65]. (**B**) Genetic design of the sensor modules used to drive the main and tuner inputs to the TES. (**C**) Experimentally measured response functions for the TES. Points denote the average of three biological replicates and error bars show ±1 standard deviation. Each line shows a fitted Hill function for a fixed tuner input (light–dark: 0.002, 0.03, 0.15, 0.43, 0.90, 2.61 RPU). Promoter activities for both the main and tuner inputs are given in relative promoter units (RPU) (**Materials and Methods**). (**D**) Flow cytometry distributions of YFP fluorescence when the tuner promoter activity is low (bottom; 0.002 RPU) and high (top; 2.61 RPU). Left and right distributions correspond to a low (0.002 RPU) and high (6.6 RPU) input promoter activity, respectively. Autofluorescence distribution is shown by the black line. (**E**) Response functions from a deterministic model of the TES (**Supplementary Text S1**). Output shown as the steady state protein level. Line color corresponds to the promoter activity of the tuner input (light–dark: 0.0001, 0.0005, 0.0025, 0.0124, 0.0617, 0.3077, 1.5340, 7.6467, 38.117, 190.00 RNAP/min). (**F**) Fraction of intersection between YFP fluorescence distributions for low (0.002 RPU) and high (6.55 RPU) inputs across varying tuner promoter activities.

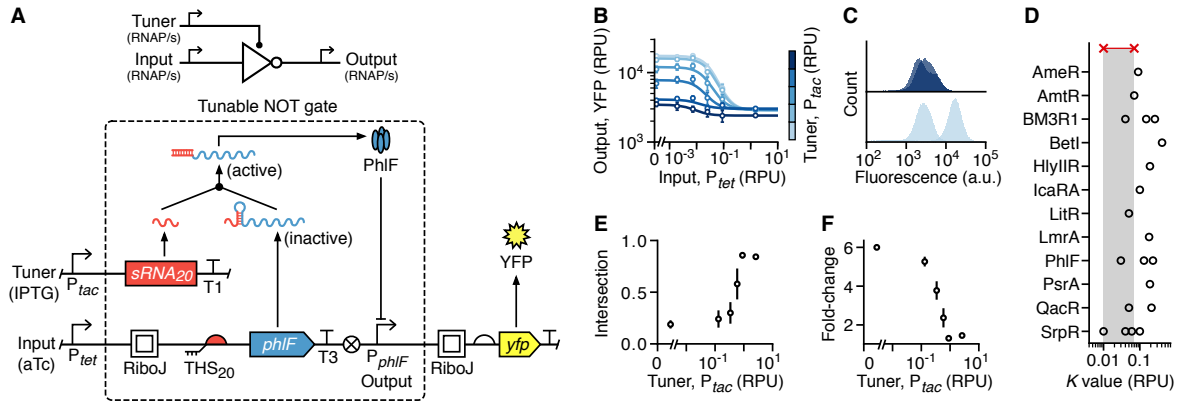

651

652 **Figure 2: Design and characterization of a tunable NOT gate.** (**A**) Schematic of the tunable
653 NOT gate (top) and genetic implementation embedding the TES (bottom). Yellow fluorescent
654 protein (YFP) expression is driven by the output promoter and T1 and T3 correspond to the
655 transcriptional terminators L3S3P11 and ECK120033737, respectively [65]. (**B**) Experimentally
656 measured response functions of the tunable NOT gate. Points denote the average of three
657 biological replicates and error bars show ±1 standard deviation. Each line shows a fitted Hill
658 function for a fixed tuner input (light–dark: 0.002, 0.03, 0.15, 0.43, 0.90, 2.61 RPU). Arrow at
659 top of plot shows range of *K* values across all fitted curves. Promoter activities for both the
660 main and tuner inputs are given in relative promoter units (RPU) (**Materials and Methods**).
661 (**C**) Flow cytometry distributions of YFP fluorescence with no autofluorescence correction from
662 the tunable NOT gate when the tuner promoter activity is low (bottom; 0.002 RPU) and high
663 (top; 2.61 RPU). Left and right distributions correspond to a low (0.0022 RPU) and high (1.51
664 RPU) input promoter activity, respectively. (**D**) Comparison of switching point (*K* value) for
665 each repressor-based NOT gate from Cello [7] (black circles) to the range achievable by the
666 tunable NOT gate (red crosses and shaded regions). (**E**) Fraction of intersection between YFP
667 fluorescence distributions for low (0.002 RPU) and high (1.5 RPU) inputs for varying tuner
668 promoter activities. (**F**) Fold-change in the median YFP fluorescence between low (0.002
669 RPU) and high (1.5 RPU) inputs for varying tuner promoter activities.

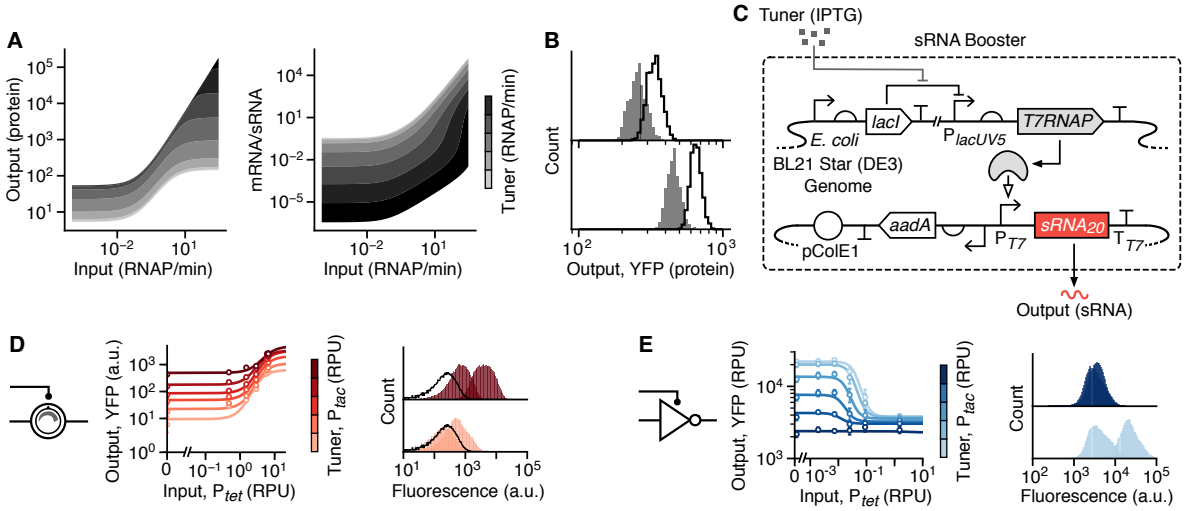

Figure 3: Increasing tuner sRNA transcription rate to improve device performance. (**A**, **B**) Results of deterministic simulations of the TES model (**Supplementary Text S1**) showing steady state protein output and THS mRNA to tuner sRNA ratio for a range of input and tuner promoter activities. Tuner promoter activities are shown in bands between 0.0001, 0.0005, 0.0024, 0.012, 0.056, 0.27, 1.3, 6.4, 31, 150 and 730 RNAP/min, respectively (light–dark). (**B**) Stochastic simulation of the same TES model (n = 10000) for low (1 RNAP/min; grey) and high (1.5 RNAP/min; green) input promoter activity. Top and bottom panels correspond to low (1.5 RNAP/min) and high (5 RNAP/min) tuner promoter activity, respectively. (**C**) Genetic design of the sRNA booster. The *T7RNAP* gene is encoded in the host genome and an additional plasmid contains a tuner sRNA expression unit. (**D**) Experimentally measured response functions (left) and flow cytometry distributions of the YFP fluorescence output (right) for the TES with the sRNA booster present. (**E**) Experimentally measured response functions (left) and flow cytometry distributions of the YFP fluorescence output (right) for the tunable NOT gate with the sRNA booster present. Points in all response functions denote the average of three biological replicates and error bars show ±1 standard deviation. Each line shows a fitted Hill function for a fixed tuner input (light–dark: 0.002, 0.03, 0.15, 0.43, 0.90, 2.61 RPU). Arrow at top of plot shows range of K values across all fitted curves. All flow cytometry distributions are shown for low (bottom; 0.002 RPU) and high (top; 2.61 RPU) tuner promoter activity, with left and right distributions corresponding to a low (0.002 RPU) and high (6.6 RPU for the TES and 1.5 RPU for the NOT gate) input promoter activity, respectively. Autofluorescence distribution is shown by the black line. Promoter activities for both the main and tuner inputs are given in relative promoter units (RPU) (**Materials and Methods**).

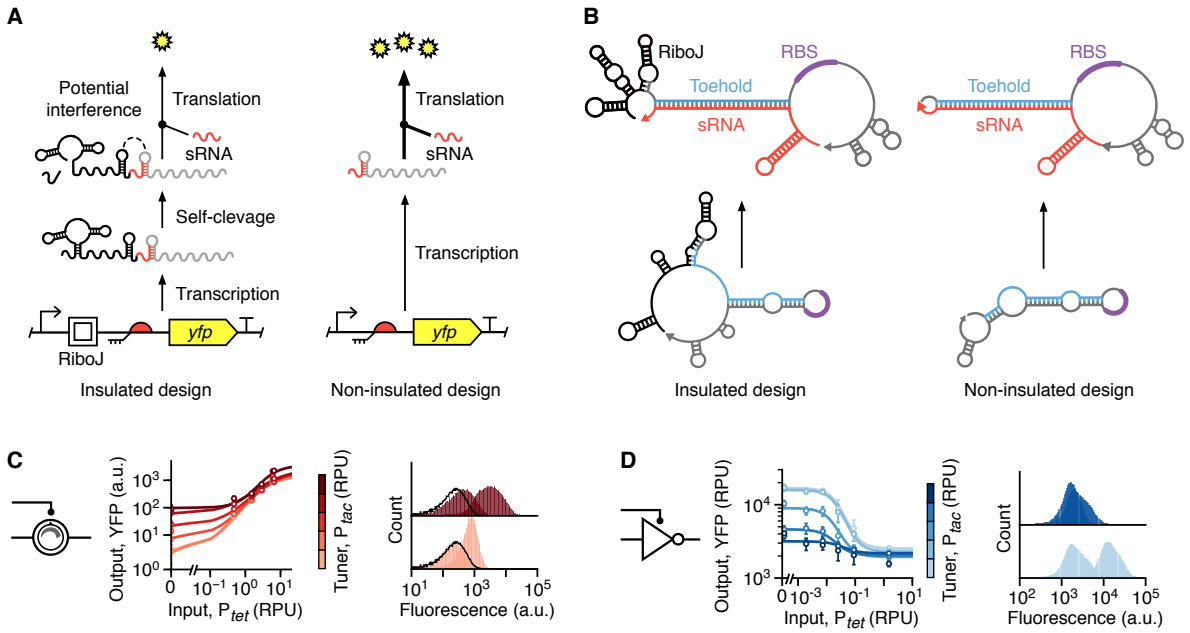

694

695 **Figure 4: Self-cleaving ribozyme insulators affect tunable device performance.** (**A**)
696 Original designs of both the TES and tunable NOT gate include a RiboJ insulating element,
697 which can potentially interfere with binding of the tuner sRNA to the toehold switch. (**B**) RNA
698 secondary structure predictions for THS alone and with complimentary tuner sRNA bound.
699 Separate structures shown when the RiboJ insulating element is present (left) and absent
700 (right). (**C**) Experimentally measured response functions (left) and flow cytometry distributions
701 of the YFP fluorescence output (right) for the TES with the RiboJ insulator removed. (**D**)
702 Experimentally measured response functions (left) and flow cytometry distributions of the YFP
703 fluorescence output (right) for the tunable NOT gate with the RiboJ insulator removed. Points
704 in all response functions denote the average of three biological replicates and error bars show
705 ±1 standard deviation. Each line shows a fitted Hill function for a fixed tuner input (light–dark:
706 0.002, 0.03, 0.15, 0.43, 0.90, 2.61 RPU). Arrow at top of plot shows range of *K* values across
707 all fitted curves. All flow cytometry distributions are shown for low (bottom; 0.002 RPU) and
708 high (top; 2.61 RPU) tuner promoter activity, with left and right distributions corresponding to
709 a low (0.002 RPU) and high (6.6 RPU for the TES and 1.5 RPU for the NOT gate) input
710 promoter activity, respectively. Autofluorescence distribution is shown by the black line.
711 Promoter activities for both the main and tuner inputs are given in relative promoter units
712 (RPU) (**Materials and Methods**).

Tables

Table 1: Performance summary of all tunable devices.

Device	Design	Dynamic range[a,b] (a.u.)		Fold-change[a,c]		Intersection[a,d]		*K* range (RPU)[g]
		Low[e]	High[f]	Low[e]	High[f]	Low[e]	High[f]	
TES	Original	333 ± 53	877 ± 695	14 ± 1.7	2.4 ± 1.2	0.78 ± 0.06	0.69 ± 0.16	–
	sRNA booster[h]	538 ± 51	2064 ± 1070	227 ± 297	5.7 ± 1.8	0.46 ± 0.04	0.35 ± 0.15	–
	Non-insulated[i]	882 ± 134	2149 ± 409	445 ± 412	31 ± 16	0.26 ± 0.07	0.27 ± 0.06	–
	Combined[j]	1550 ± 209	1712 ± 584	1236 ± 613	66 ± 54	0.15 ± 0.04	0.22 ± 0.04	–
NOT gate	Original	17280 ± 1273	3512 ± 286	6.0 ± 0.1	1.5 ± 0.1	0.19 ± 0.04	0.84 ± 0.02	0.01–0.07
	sRNA booster[h]	22040 ± 1601	2170 ± 654	5.8 ± 0.3	0.9 ± 0.3	0.13 ± 0.07	0.85 ± 0.02	0.01–0.06
	Non-insulated[i]	17466 ± 1926	4061 ± 827	6.8 ± 0.3	2.6 ± 0.4	0.11 ± 0.03	0.56 ± 0.08	0.02–0.04
	Combined[j]	27751 ± 3104	2383 ± 165	6.0 ± 0.6	0.9 ± 0.1	0.08 ± 0.05	0.90 ± 0.03	0.003–0.02

a. Average values are shown ± 1 standard deviation calculated from flow cytometry data for three biological replicates.

b. Dynamic range calculated as the absolute difference in YFP fluorescence between low and high inputs (0.002 and 6.6 RPU for the TES, and 0.002 and 1.5 RPU for the NOT gate, respectively).

c. Fold-change in YFP fluorescence (corrected for cell autofluorescence) for low and high inputs (0.002 and 6.6 RPU for the TES, and 0.002 and 1.5 RPU for the NOT gate, respectively).

d. Fraction of intersection between the flow cytometry YFP fluorescence distributions for low and high inputs (0.002 and 6.6 RPU for the TES, and 0.002 and 1.5 RPU for the NOT gate, respectively) (**Materials and Methods**).

e. Performance measured for a low tuner input (0.002 RPU). This is the expected promoter activity of the P_{tac} promoter in our designs.

f. Performance measured for a high tuner input (2.61 RPU). This is the expected promoter activity of the P_{tac} promoter in our designs.

g. Range of *K* values from Hill functions fitted to experimental data.

h. Original designs (**Figures 1A** and **2A**) with the sRNA booster system (**Figure 3E**).

i. Design has the RiboJ insulating element removed (**Figure 4A**).

j. Design has the RiboJ insulating element removed (**Figure 4A**), and sRNA booster system present (**Figure 3E**).